PAPER

Electrochemical-acoustic time of flight: in operando correlation of physical dynamics with battery charge and health†

A. G. Hsieh,‡[ab] S. Bhadra,‡[bc] B. J. Hertzberg,[ab] P. J. Gjeltema,[a] A. Goy,[c] J. W. Fleischer[c] and D. A. Steingart*[ab]

We demonstrate that a simple acoustic time-of-flight experiment can measure the state of charge and state of health of almost any closed battery. An acoustic conservation law model describing the state of charge of a standard battery is proposed, and experimental acoustic results verify the simulated trends; furthermore, a framework relating changes in sound speed, via density and modulus changes, to state of charge and state of health within a battery is discussed. Regardless of the chemistry, the distribution of density within a battery must change as a function of state of charge and, along with density, the bulk moduli of the anode and cathode changes as well. The shifts in density and modulus also change the acoustic attenuation in a battery. Experimental results indicating both state-of-charge determination and irreversible physical changes are presented for two of the most ubiquitous batteries in the world, the lithium-ion 18650 and the alkaline LR6 (AA). Overall, a one- or two-point acoustic measurement can be related to the interaction of a pressure wave at multiple discrete interfaces within a battery, which in turn provides insights into state of charge, state of health, and mechanical evolution/degradation.

Broader context

Recent advances in the mechanical understanding of electrochemical energy storage devices based on stress/strain investigations have provided significant improvements in battery systems and materials. To date, the field has lacked a non-invasive, field-deployable method for monitoring these complex mechanics in practical cells. Here, we show a simple model and experiment together as a potentially universal in operando, field-deployable tool for determining the mechanical evolution, state-of-charge and state-of-health of any closed battery using acoustic time of flight analysis. The technique is tested against off-the-shelf lithium ion and alkaline batteries: the acoustics correlate strongly to state-of-charge and state-of-health on a second-to-second basis. This technique provides new physical measurements into two completely different batteries that were sold by the billion in 2014 alone. We show that property distributions of batteries can be determined in unmodified full cells in real time, in operando, without electrodes, and using only a single point of contact. In previous studies these measurements have been related, via complex lab equipment, to rapid battery fade as well as safety concerns. This work outlines simple methods to greatly increase these types of measurements in a manner that can be readily embedded into battery management systems.

Introduction

The very quality that makes batteries interesting for academic research is concurrently a source of frustration for their practical implementation: each chemistry has a specific physical fingerprint, which leads to unique cycling behaviors, desired or otherwise.

[a] Department of Mechanical and Aerospace Engineering, Princeton University, Princeton, New Jersey 08544, USA. E-mail: steingart@princeton.edu

[b] Andlinger Center for Energy and the Environment, Princeton University, Princeton, New Jersey 08544, USA

[c] Department of Electrical Engineering Princeton University, Princeton, New Jersey 08544, USA

† Electronic supplementary information (ESI) available. See DOI: 10.1039/c5ee00111k

‡ These authors contributed equally to this work.

The standard suite of electrochemical tools provides a window into the physical changes of each chemistry, but it is at best an abstract representation of the physical changes occurring in the cell. In situ and in operando optical,[1,2] electron,[3–5] X-ray[6–9] and neutron scattering[10–12] methods have provided rich data which describe the behavior of idealized cells, but with few exceptions[13–16] it has been difficult to directly probe the physical changes in conventional batteries. This is a true detriment to the field, as scaling up cells is not a trivial linear exercise: physical insights into large-scale cells, without the need for expensive equipment such as a synchrotron light source, would be welcome both in academia and in industry.

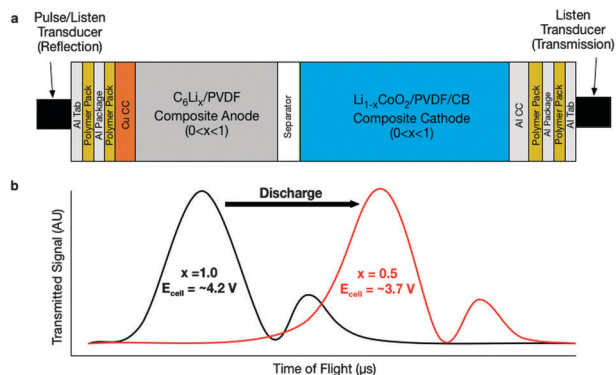We present the framework for a non-invasive, in operando method that is able to extract a rich data set from numerous

Fig. 1 Ultrasonic interrogation of a representative battery. (a) Schematic representation of the experimental/modeling configuration, showing a typical battery with the various packaging, current collector, electrode, and separator layers as well as the two acoustic transducers (pulse/listen and listen) used for ultrasonic interrogation. (b) Example illustration of the increase in time of flight (ToF) of the transmitted signal as a function of SOC that occurs during discharge; this shift is a result of the changes in electrode densities as the SOC (*i.e.*, Li content, x) changes.

battery designs by exploiting a physical truth that underlies all closed electrochemical systems: they are, by design, reactors which redistribute density as a function of state of charge (SOC) in the ideal case and, additionally, as a function of state of health (SOH) in reality. Regardless of the reaction mechanism (intercalation, dissolution/reprecipitation, phase change, *etc.*), the density and elastic modulus of an electrode changes as a function of its SOC, and this distribution as well as the rate of change of this distribution can act as a fingerprint of SOH. For what we believe is the first time in the literature, in the present study we use acoustic ultrasonic transducers to probe the changes in density distribution in real time, and provide a model which describes how ultrasonic echoes within an arbitrary cell change as a function of the SOC. The concept for this approach is illustrated for an example cell in Fig. 1. In this article we discuss a simple method that may be used with one or two transducers to characterize SOC and SOH. Beyond correlations between density and acoustic signal amplitude, acoustic attenuation will also change as a function of the effective modulus of each layer in the battery.

Recently, there has been significant work correlating static strain at a macroscopic level to SOC and SOH in batteries which exhibit significant volume changes.[17–21] In some cases, the macroscopic strain can be exploited as an actuator.[22] Acoustics have been employed to detect emissions from macroscopic cracking,[23–26] and microscopic AFM measurements[27,28] and models have been developed to determine the causes and critical aspects of "electrochemical shock."[29–32] While there have been efforts in ultrasonic imaging of full cells, they have focused on the examination of irreversible failure through delamination and cracking.[33–35] To the best of our knowledge, no efforts have correlated slight-to-moderate mechanical degradation or SOC with ultrasonic interrogation. In this work, we employ acoustic methods that were developed for flaw detection of bulk metals and welds[36–38] to accurately correlate state of charge within a battery to subtle changes within materials and between layers.

Methods

Computational

A standard 1D acoustic conservational law model was used to explore the effect of density and modulus on the echoing behavior of an ultrasonic pulse, based on the mismatch in sound speed between adjacent layers within a battery. The speed of sound, c, in a solid material can be calculated from the Newton–Laplace equation:

$$c = \sqrt{\frac{E}{\rho}} \qquad (1)$$

where E is the elastic modulus, and ρ is the density. The conservation laws package (Clawpack)[39] with the Riemann acoustics solver was used to simulate a full battery stack (Fig. 1a) using python (*via* pyclaw). In one dimension, the governing continuity equations are:

$$p_t + E \cdot u_x = 0 \qquad (2)$$

$$u_t + \frac{1}{\rho} \cdot p_x = 0 \qquad (3)$$

where p is the pressure, u is the wave velocity, and the subscripts x and t imply spatial and temporal variation, respectively. Values for the densities and elastic moduli of the electrode components were assembled from the references in Table 1; the densities for $LiCoO_2$ and graphite are listed as a function of Li content.

In modeling the electrodes (assuming 80% active material, 10% conductive additive, 10% binder), to a first approximation the effective densities of the composite anode and cathode can be estimated from a mass-fraction weighted sum of the densities of the individual components. Similarly, the effective moduli of the anode and cathode layers can be estimated from a volume-fraction weighted sum of the component moduli. Additionally, a composite can be considered ultrasonically homogeneous if the particles are much smaller than the acoustic wavelength, which has been confirmed by both experimental and theoretical evidence.[42] For the sake of simplicity, all of these assumptions were used in our simulations. In future work, we will examine more complex models of granular materials, such as the Kelvin–Voight relationship. This is a non-trivial exercise, as the modeling of acoustic impedance and attenuation in packed-particle beds is still an active area of research within the acoustic community, with many questions posed decades ago still unanswered.[43,44] This said, our current model captures a qualitatively meaningful relationship between state of charge and acoustic behavior.

Table 1 Densities and elastic moduli of electrode components for acoustic simulation

Material	Density (kg m^{-3})	Modulus (GPa)	Citation
LiCoO$_2$	4800–5150	168.0	40
Graphite	2260–2500	27.6	22
Al	2700	69.0	41
Cu	8960	117.0	41
PVDF	1800	2.0	41
Carbon black	1900	25.0 (est.)	41

Changes in the states of charge and lithium content in each electrode during cycling were determined *via* a Dualfoil simulation.[45] The lithium content for each time step was extracted from the Dualfoil output file and was then used to estimate the density changes in each electrode based on values from studies by Reimers and Dahn.[40] The changes in density were then fed into Clawpack to simulate the resulting change in acoustic behavior as a function of state of charge. As a first approximation, the modulus was held constant; however, in future studies it may be possible to determine elastic modulus from the acoustic measurements.

The Dualfoil input files were not modified from the standard li-ion.in input files created with the package. Within Python, using the pyclaw library, the input file from the Dualfoil simulation was used to define the geometry of the cell, and extra layers representing current collectors and external packaging were added.

Experimental

Electrochemical-acoustic time of flight (EAToF) experiments were performed on a $LiCoO_2$/graphite pouch cell, a cylindrical $Li(NiCoAl)O_2$/graphite 18650 cell, and Zn/MnO_2 alkaline AA cells (Duracell and CVS Brand). Specific cell information is provided in the ESI.†

An Olympus EPOCH 600 ultrasonic pulser-receiver was used with two 2.25 MHz transducers: one in pulse-echo (reflection) mode and the other in transmission mode. This allowed the measurement of reflected and transmitted signals through the cell. A small amount of glycerin was used to ensure a reliable acoustic interface between the transducers and the cell, and the transducers were held in place with light pressure using a custom-designed 3D printed holder (Formlabs Form1+). No modifications were made to the cells. Custom Python software was written to control the EPOCH through Pithy.[46] The applied pulse was 50 ns long and its transmission/echo behavior was measured out to 20 µs; measurements were taken every 30 seconds.

To test the cells electrochemically, galvanostatic cycling protocols were used with a Neware BTS-3000 cycler. For the $LiCoO_2$/graphite and $Li(NiCoAl)O_2$/graphite cells, a C/2.5 cycling rate was used, with 30 m rest in between each charge and discharge step. For the alkaline AA cells, single discharge steps at C/20, C/10, and C/5 rates were used. The Neware was time-synchronized with the EPOCH, and all data analysis was performed with Python.

Results and discussion

Movie S1 (ESI†) demonstrates a simulated pulse passing through a one-stack cell, and the resulting reflection and transmission gauge readings. As the initial pulse passes through each interface, some fraction of the wave is transmitted and some is reflected, depending on the degree of mismatch in the sound speed *c* between adjacent layers and whether *c* increases or decreases from one layer to the next; additionally, the wave attenuates (*i.e.*, loses energy) as it passes through the bulk region

of each layer.[47] As each interface is an opportunity for the pulse to split, as shown in the movie, the acoustic behavior of the cell quickly becomes complicated as each new wave interacts not only with interfaces (creating even more waves) but also with each other. The complex interplay of sound speed mismatches as well as constructive and destructive interference between the waves creates the observed reflection and transmission traces. Furthermore, as the time of flight (ToF) increases, the sound waves become increasingly dampened due to dissipation and the increasing number of encountered interfaces. The result is an "echo chamber" effect for the longer ToF waves.

To simulate the effect of galvanostatic cycling on the echoing behavior of the cell, a simple 1D stack of the regions listed in Table 1 was created in the standard cell geometry defined by Dualfoil.[45] For a series of time steps, the changes in electrode densities were calculated as a function of SOC using Dualfoil, which were then fed into Clawpack to determine the resulting acoustic behavior of the cell. The snapshots were composited to obtain the time-resolved simulated acoustic results shown in Fig. 2. This simulation illustrates that during cycling, there is a measurable shift in the ToF of the primary transmission gauge reading (indicated by arrow 1) as well as a change in the signal intensity, which are both clearly functions of the SOC of the battery (*i.e.*, density changes in the anode and cathode due to
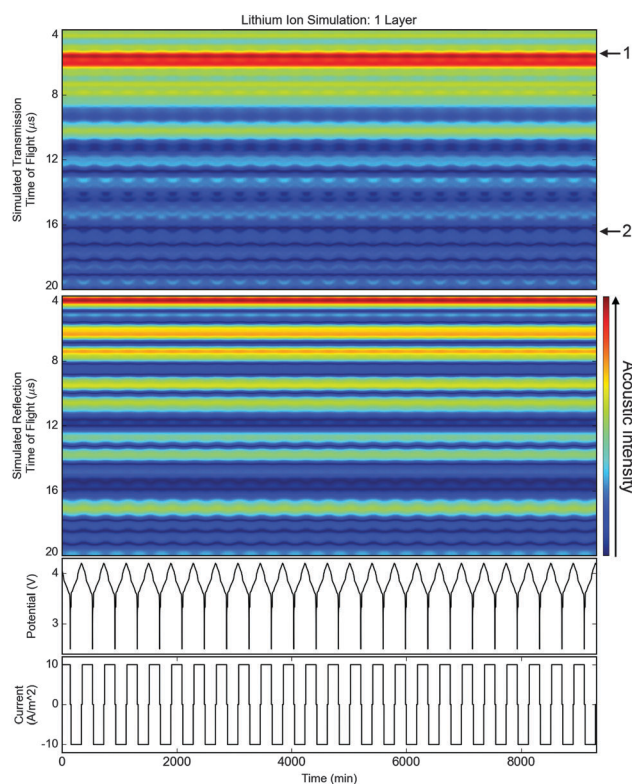

Fig. 2 Simulation of echo behavior as a function of SOC. Clawpack–Dualfoil simulation of the ToF of acoustic echoes (transmission and reflection modes) in a simple, single 1D battery stack as a function of SOC; as shown in the scale bar on the right, blue to yellow red indicates increasing acoustic intensity. Also shown are the corresponding cell potential and applied current density profiles. Arrows 1 and 2 are discussed in the text.

lithium intercalation/deintercalation). In addition to becoming increasingly dampened, the later transmission signals (*e.g.*, the trace indicated by arrow 2) display an enhanced shift in ToF between the charged and discharged states. Similar trends are observed in the reflection data.

To simulate cylindrical and prismatic cell designs, cells consisting of multiple stacks of electrodes were run through the Clawpack–Dualfoil simulation, and Fig. S1 (ESI†) demonstrates the effect of cell folding/winding on the output acoustic signals. We see that as the size of the simulated cell is increased to 4 electrode stacks, the acoustic behavior becomes increasingly complex, as there are more and more interfaces for the waves to pass through, resulting in a progressively increasing number of waves echoing and interfering with one another. It is worth noting that commercially available cells generally contain many more layers than this, which, as we will see further below, results in even more complex acoustic behaviors.

Ultrasonic time of flight analysis was performed on a commercial LiCoO$_2$/graphite pouch cell during galvanostatic cycling: the reflected and transmitted signals were measured every 30 seconds during cycling, providing acoustic snapshots of the cell as a function of time. Time-resolved acoustic results were visualized by compositing these snapshots into a two-dimensional intensity image of cycle time against ToF data (selected data shown in Fig. 3a and b, full data set shown in Fig. S2, ESI†). These composite images demonstrate both the change in intensity for each acoustic wave received by the transducers as well as the ToF shift in each wave during cycling. Focusing on the transmission data (Fig. 3a), we see that each

ToF peak shifts towards lower values and higher intensities during charge, and towards higher values and lower intensities during discharge. Furthermore, a comparison of transmission peaks 1, 3, and 10 shows that the later (*i.e.*, longer ToF) peaks display a more pronounced shift in ToF position between the charged and discharged states, and are in general less intense. Similar trends are also observed in the reflection data (Fig. 3b). These experimental trends are reminiscent of the shifts in ToF and intensity observed in the Clawpack–Dualfoil simulations. While there are strong correlations between the simulated SOC–ToF relationship and the overall experimental ToF trends, due to the assumptions made, our model does not capture many of the nonlinear intercalation-driven changes that are known to occur. Nevertheless, we are able to draw several meaningful correlations between the acoustic and electrochemical results.

For each ToF snapshot, we calculated the total transmitted and reflected signal amplitudes by summing the intensity across the entire 0–20 µs ToF window, shown in Fig. 3c. As the battery is discharged, acoustic absorption increases (*i.e.*, the transmitted and reflected intensities decrease), with a notable, but repeatable, exception at the end of discharge at a cell potential <3.5 V, where there is a dramatic increase in the signal intensities (dotted oval, Fig. 3c). We believe this is driven primarily by the capacity-limited cathode: near 0% SOC, LiCoO$_2$ approaches a hexagonal-to-monoclinic phase transformation, dramatically altering both the modulus and density of the cathode.[40] Following discharge, as the applied current is removed during the rest step, we see the cell potential increase as local lithium gradients relax, which in turn relaxes any build-up in lattice strain due to the
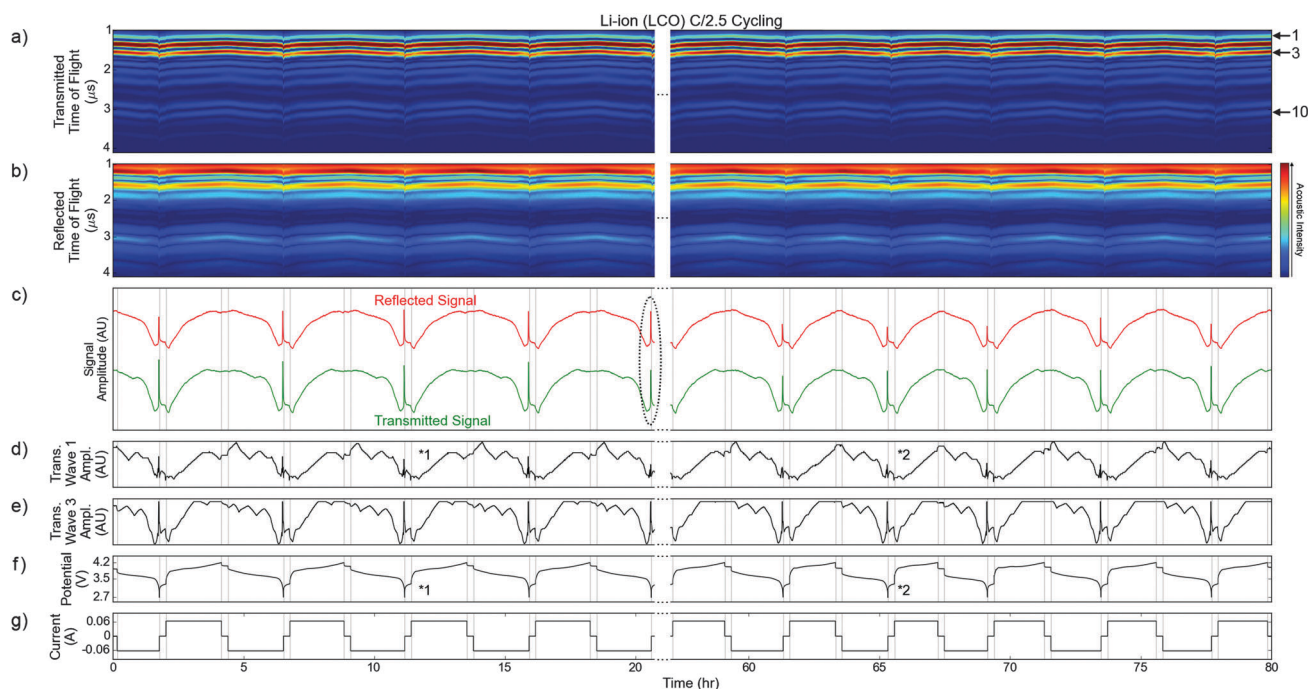
Fig. 3 Acoustic behavior of a LiCoO$_2$/graphite prismatic cell. (a, b) ToF maps for transmission and reflection modes, respectively, (c) total reflected (red) and transmitted (green) signal amplitudes, (d, e) traces for the amplitudes of transmitted waves 1 and 3, respectively, (f) cell potential, and (g) applied current as a function of cycling time. The vertical gray lines in panels c–g represent transitions between charge, discharge, and rest steps; arrows 1, 3, and 10, the dotted oval, as well as markings *1 and *2 are discussed in the text.

aforementioned phase transformation, and the acoustic signal intensities decrease accordingly. When the cell is charged, the acoustic intensities decrease slightly as the phase transformation is reversed, followed by a steady increase in the intensities with increasing SOC. At the end of charge, there is a slight, repeatable increase in acoustic absorption when the cell potential is >4 V. We believe that this is also driven primarily by the cathode, as near 100% SOC, the $LiCoO_2$ undergoes a two-phase staging reaction which changes its density significantly.[48]

Particularly interesting is the information contained within individual ToF peak traces. Fig. 3d and e show the amplitudes of transmitted waves 1 and 3, respectively, and we see that while their general trends are similar to one another and to the total amplitude, there are subtle differences between them. Furthermore, amplitude changes in the individual waves follow different trends with cycle number. For example, if we focus on the amplitude of transmitted wave 1 during the charge step, there is a peak in the 3rd cycle (marked by *1, Fig. 3d) that disappears by the 15th cycle (*2, Fig. 3d). These changes seem to be a strong predictor of the cell accepting less charge before the 4.2 V cut-off potential, evident from the respective potential profiles and charging times. We note that the cell recovered some capacity before continuing the trend toward degradation, and that similar types of correlations between amplitude and capacity can be made for other individual wave traces as well. While the changes are slight, comparison of the overall recovered acoustic signal with the signal recovered for specific ToF traces nevertheless reveals repeatable correlations with SOH. This is intriguing as it enables the development of detailed acoustic

models in which hypothetical electrode degradation mechanisms can be compared to the performance of a practical cell. The development of such models is not a trivial endeavor and is currently under investigation.
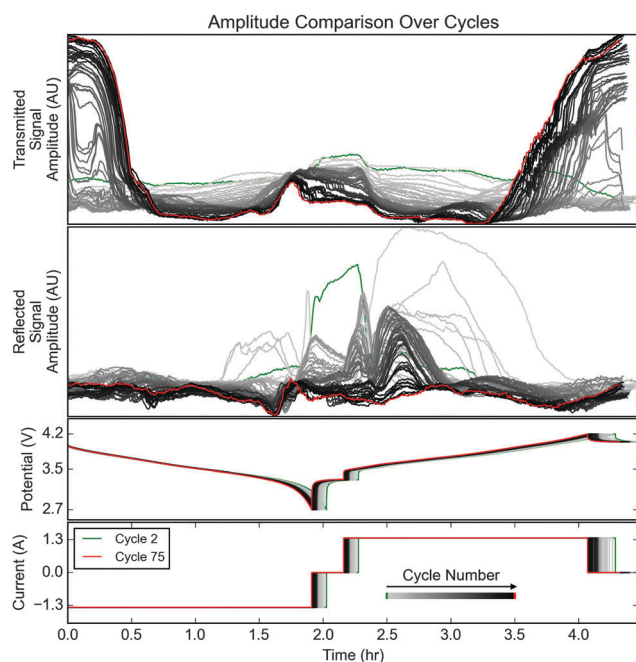
To evaluate the influence of cell construction and material distribution on acoustic behavior, ultrasonic ToF analysis was performed on a $Li(NiCoAl)O_2$ (NCA)/graphite 18650 "jelly roll" cell during galvanostatic cycling starting from a fresh state (selected data shown in Fig. 4, full data set in Fig. S4, ESI†). As shown in the ToF maps (Fig. 4a and b), the acoustic behavior is significantly more complicated in the 18650 cell than in the prismatic cell (Fig. 3). Based on the simulated ToF maps from Fig. S1 (ESI†), this increase in acoustic complexity is expected, as cells of this design typically consist of 15 to 25 layered windings.[41] The total reflected and transmitted signal intensities (Fig. 4c) as a function of SOC varies significantly over the first 11 cycles, after which the acoustic behavior stabilizes; this indicates the presence of an initial "formation" period, which is consistent with previous efforts on the acoustic emission of batteries.[25,27] As cycling continues, the total transmitted signal at the end of charge becomes increasingly large, as after ∼27 cycles new peaks between 8 and 12 μs begin to appear in the transmission ToF map (Fig. 4a, indicated by the white arrow).

New to the literature is a demonstration of the evolution of the acoustic signal attenuation (as estimated from the fraction of the interrogating (input) pulse measured by the transmission and reflection transducers) of a lithium ion cell, as a function of cycle number. Fig. 5 shows a cycle-by-cycle comparison of the acoustic behavior of the NCA/graphite 18650 cell, in which the
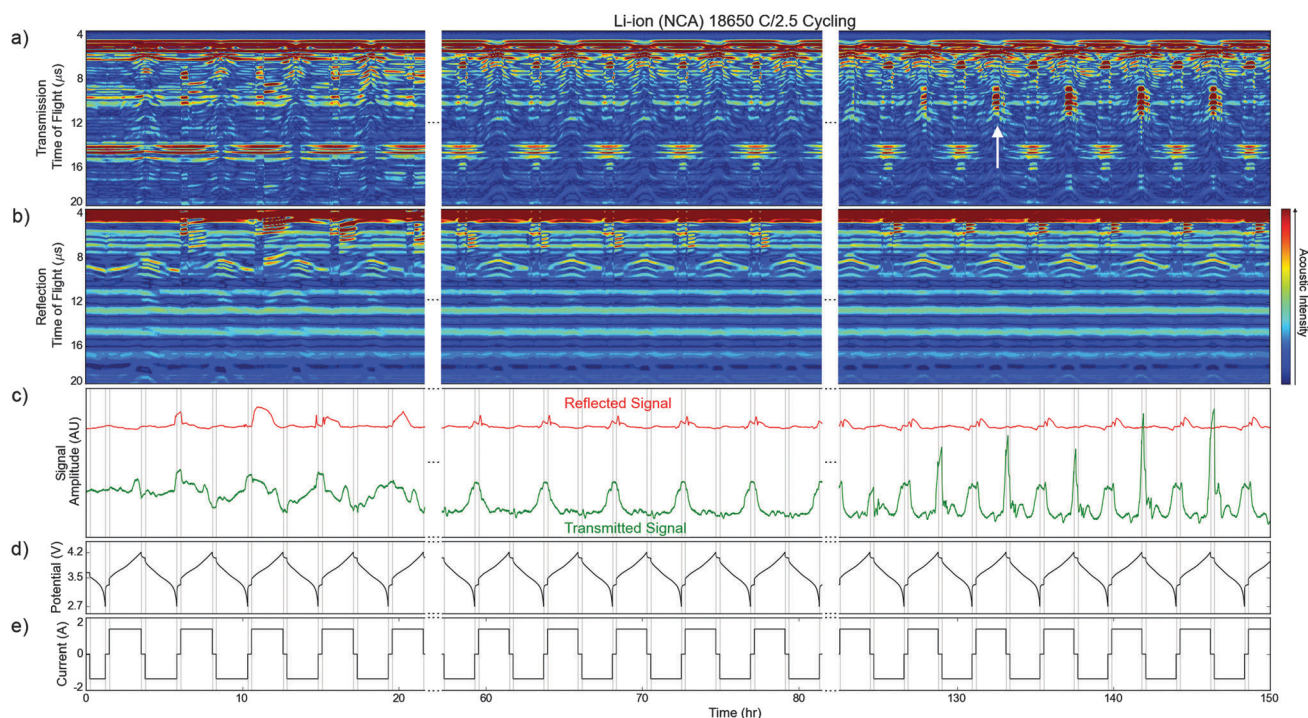
Fig. 4 Acoustic behavior of an NCA/graphite 18650 cell from cycle 1 to 34. (a, b) ToF maps for transmission and reflection modes, respectively, (c) total reflected (red) and transmitted (green) signal amplitudes, (d) cell potential, and (e) applied current as a function of the cycling time. The vertical gray lines in panels c–e represent transitions between charge, discharge, and rest steps. The white arrow at ∼132 h in panel a is discussed in the text.

total transmitted and reflected signal amplitudes are separated by cycle number and superimposed. There are a few interesting shifts, both at the end of discharge and at the end of charge. In particular, attenuation of the acoustic signal decreases significantly and consistently near the end of discharge, as evidenced by the increase in reflected and transmitted signal intensities. Most likely, this is a compliance change related to the gradients of Li distribution within active cathode particles. Diffusion limitations may lead to a scarcity or excess of lithium near the surface of a particle, resulting in a dramatic change in its mechanical properties (in a fashion similar to that described by Woodford *et al.*[30]); this can either create local disorder by increasing lattice mismatch with the more-lithiated regions of the particle, leading to enhanced phonon scattering, or may simply result in an increase in lattice stiffness. This effect is likely caused by the cathode, as commercial lithium ion cells contain excess graphite to prevent lithium plating during charge.[41] During the rest step the local lithium gradients relax, which in turn relaxes the lattice strain, and the acoustic signal attenuation increases slightly as a result. Attenuation of the acoustic signal becomes increasingly strong at the end of charge with increasing cycle number. Similar to the discharge step, this suggests dramatic changes in the mechanical properties of electrodes, which is in agreement with static mechanical analysis of electrodes.[17–19] Similar trends exist in the pouch cell after 50 cycles, but as the 18650 cell geometry is significantly more complicated we hesitate to assert more than correlations between acoustic behavior and states of charge and health.

While our computational model generally describes the experimentally observed acoustic phenomena in lithium-ion batteries, there are notable differences that demand further investigation. First, the 90° phase shift between reflected and transmitted waves in the model is not seen in either lithium-ion cell tested; we believe an additional layer may be present in the cells that may "rephase" the signal, however a more detailed consideration of individual layer effects is required. Second, our model did not account for modulus changes within the electrodes during cycling (though they are likely present), which probably contributes to the more dramatic shifts in acoustic signal delay and attenuation. Third, our model only considered density changes due to lithium intercalation and de-intercalation; in reality, density and modulus changes due to phase transformation, staging effects, *etc.* also need to be considered. Fourth, due to the one-dimensional nature of our model, heterogeneities in current density throughout the electrodes during cycling were not accounted for. Furthermore, assumptions were made regarding electrode porosity and acoustic homogeneity. Nonetheless, the model presented herein does begin to describe the complex but repeatable acoustic response within the batteries. This is an important point that bears emphasizing: though our model does not capture many of the detailed acoustic and electrochemical processes, it nevertheless captures much of the general behavior observed experimentally. This clearly shows the feasibility of the electrochemical-acoustic approach for SOC and SOC determination, and lays the groundwork for future studies.

Ultrasonic time of flight experiments were also performed on commercial $Zn–MnO_2$ alkaline AA cells from two different manufacturers (Duracell and CVS) during galvanostatic discharge. As shown in Fig. 6, the two alkaline cells exhibited similar overall acoustic responses, however there are notable differences between them: the transmitted signal of the Duracell was initially greater than that of the CVS cell. We attribute this to the Duracell battery design, specifically to the delamination of the Duralock™ corrosion protection layer. This proprietary polymeric coating on the Zn anode particles increases mechanical contact between them and results in the larger initial transmission signal compared to the CVS cell. When the discharge current was applied, the acoustic signal attenuated in both the Duracell and CVS brand batteries; this effect was more pronounced in the Duracell (see Fig. S5, ESI† for more details). In both cells we believe this initial attenuation is due in part to the nature of the discharge reaction: in an alkaline (*e.g.* KOH) electrolyte, solid Zn is stripped from the surface of individual particles and aqueous zincate ($Zn(OH)_4^{2-}$) ions form. This causes the Zn particle network to become less packed, which in turn attenuates the acoustic signal. In the Duracell, though, we also attribute some of the acoustic attenuation to the disintegration of the Duralock™ coating. This is corroborated by electrochemical impedance spectroscopy (EIS), shown in Fig. S6 (ESI†), in the form of a large drop in total cell impedance after the onset of discharge.

As discharge continues in both cells, the transmission peak traces between 8 and 20 µs undergo shifts in ToF that follow Nernstian-like patterns, similar to the changes in cell potentials, and the acoustic signal intensities are greatly enhanced by the

Fig. 5 Cycle-to-cycle analysis of the acoustic behavior of an NCA/graphite 18650 cell. Evolution of (from top) the transmitted and reflected signal amplitudes, cell potential, and applied current as a function of cycling time for cycles 2 through 75 from the acoustic/electrochemical data in Fig. 4. For each plot, the first cycle is indicated in green, with subsequent cycles shown as progressively darker shades of grey and the final cycle indicated in red.
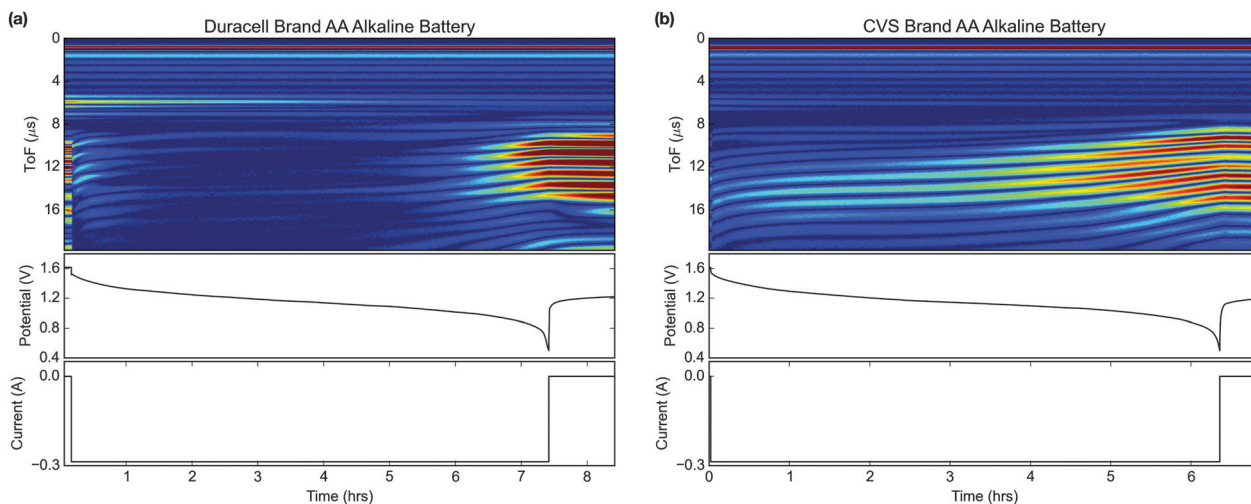
Fig. 6 Acoustic behavior of two brands of alkaline AA cells. (a) Transmission ToF map of an ultrasonic pulse in a Duracell alkaline AA, with the corresponding cell potential and current profiles. (b) Transmission ToF map of an ultrasonic pulse in a CVS brand alkaline AA, with the corresponding cell potential and current profiles. Both cells were discharged at 280 mA, corresponding to a C/10 rate.

end of discharge. This is likely due to the formation of solid ZnO as the saturation limit of $Zn(OH)_4^{2-}$ is reached.[49,50] Eventually, near the end of discharge, the ZnO creates a percolated network of ZnO within the anode, causing the transmitted signal to increase dramatically.[51] In the Duracell, however, we note that after the current is applied the signal intensity decreases until about halfway through the discharge step before it begins to increase. This is distinct from the CVS cell, in which (after the initial attenuation) the transmitted signal increases monotonically throughout discharge. We believe this difference is a result of the Duralock™ corrosion protection layer as well as proprietary electrolyte additives used by Duracell to prevent corrosion and increase ZnO solubility. Indeed, upon dissection of fresh batteries, we found Zn from the Duracell to be more lustrous than that from the CVS cell, indicating less ZnO in the Duracell initially.

There is also a set of ToF peaks between 4 and 8 μs that is more pronounced in the Duracell battery than in the CVS battery. We attribute this observation to differences in the cathode materials; the Duracell cathode appears to have smaller, more densely packed particles than the CVS cathode, as shown in confocal microscope images in Fig. S7 (ESI†), which would result in a more mechanically-connected network. In both cells, these peaks gradually fade in intensity (but do not shift in ToF) during discharge. This is possibly due to the expulsion of aqueous electrolyte from the anode to the cathode during discharge, which has been observed *via in situ* neutron tomography by Riley *et al.*[52] The increase in cathode water content would cause the relevant transmission peaks to attenuate relative to a drier cathode. After discharge, the relaxation behavior appears to be similar for both cells. These results are particularly noteworthy because they show that acoustic time of flight measurements can be sensitive enough to detect differences in manufacturing processes between multiple brands of the same battery chemistry.

To demonstrate the effect of discharge current on the acoustic behavior of alkaline batteries, Duracells were discharged at different rates. As shown in Fig. S8 (ESI†), the cells show a

marked difference in their acoustic transmission profiles as a function of discharge rate. The morphology and spatial distribution of ZnO in alkaline batteries is known to depend on discharge rate, as shown by Horn *et al.*,[53] so the different ToF profiles are probably due to the influence of discharge rate on formation of ZnO and thus mechanical properties of the full cell. Higher discharge rates result in ZnO forming predominantly in the regions closest to the anode/separator interface, while lower discharge rates result in a more uniform distribution of ZnO formation throughout the anode. Thus, cells that are discharged more slowly develop a ZnO network that is more percolated (and thus transmits sound more readily) than cells that are discharged more quickly.[51] A detailed understanding of the structural and mechanical changes that are responsible for the ToF behavior in alkaline cells will be addressed further in a later publication.

Conclusions

Electrochemical-acoustic time-of-flight experiments were performed on several batteries, including a $LiCoO_2$/graphite pouch cell, a cylindrical $Li(NiCoAl)O_2$/graphite 18650 cell, and on two types of Zn/MnO_2 alkaline AA cells. Our results demonstrate strong correlations between SOC and the density distribution within a cell, as determined by the acoustic measurements, and suggest that this is an effective analysis technique regardless of battery chemistry and form factor. Beyond SOC, the changes in density are indicative of underlying physical processes occurring in the electrode materials during cycling, such as the "formation" period in the as-received LiNCA/graphite 18650 cell as well as the degradation of the $LiCoO_2$/graphite pouch cell. Changes in the ToF echo profiles and acoustic signal amplitudes as a function of cycle number appear to be key indicators of critical phenomena occurring within the battery, including changes in intraparticle and interparticle

stress and strain, as well as the formation and removal of critical surface layers (SEI/passivation, artificial and natural). Such correlations suggest that the electrochemical-acoustic data can be used to determine SOH.

We have shown through acoustic modeling that the key constituents of sound speed, *i.e.*, bulk modulus and density, are closely related to the observed changes in the measured acoustic signal during electrochemical cycling. These properties, to date, have been exceptionally difficult to determine *in situ* or *in operando*. It is important to note that our model did not include many of the non-linear physical process that are known to occur during cycling. Furthermore, commercial cells typically contain many more layers than were included in our simulations. As such, the model that we presented is not accurate enough for layer-by-layer decoupling of the experimental ToF data, nor can it be used as a predictive tool (the development of such models is not a trivial endeavor, as it requires exact layer-by-layer control when constructing cells in the lab). Nevertheless, our model was able to qualitatively capture much of the acoustic behavior that was observed experimentally. This is a clear indication of the feasibility of our electrochemical-acoustic approach, and the work presented herein lays the groundwork for future studies to refine the details of the model and our understanding of the technique.

The electrochemical acoustic ToF method is powerful because it provides a fingerprint of a battery's chemistry and geometry. While a more detailed model is required to decouple the individual effects, this is a tool that is comparable to EIS in insight and utility, where a well-designed model in conjunction with experimental data provides fundamental insights. The quality of the acoustic data is complemented by the universal applicability of this approach. While ultrasonic ToF analysis cannot directly probe chemical and structural properties in the same way that neutron, X-ray and electron methods can, it is still able to provide physical insights that are not possible with standard electrochemical equipment at a fraction of the cost of photonic interrogation methods. Unlike EIS and other inline electrochemical test methods, acoustic ToF analysis can be done without electrical contact and even with only one point of physical contact if operating in pulse/echo mode. Furthermore, unlike photonic characterization, this method can be applied readily to commercial off-the-shelf cells of very different chemistries and form factors.

This simple, high-speed technique that provides heretofore unmeasurable physical correlations for large-scale complex batteries, as well as physical insights that have only previously been available through high-energy X-ray analysis. The technique is effective across all battery technologies because it exploits a common thread to all cells: critical manufacturing control of layers and the shifting of mass within the cell. While different batteries will exhibit different acoustic progressions during operation, the same theory should be broadly applicable. In this article we demonstrated new physical insights to a substantial majority of the worlds batteries, namely the nearly 2 billion cells manufactured in 2014 considering both AA Alkaline and 18650 Li-ion batteries.[54–56] To date, ultrasonic methods for battery

analysis have been limited to careful laboratory studies or analysis of dramatic failure, and we have shown here that they can be used broadly to learn and probe much more about all types of cells. The methods can be applied to batteries during operation, using equipment that can be readily integrated into electric vehicles and devices as small and simple as a cell phone (*e.g.* basic signal processing electronics and simple piezoelectric transducers). This provides rich opportunities for multiplex testing within a lab environment as well as field analysis of the physical properties of batteries, all without any modification to the cells themselves.

Competing financial interests

The authors declare no competing financial interests.

Acknowledgements

References

1 J. W. Gallaway, D. Desai, A. Gaikwad, C. Corredor, S. Banerjee and D. Steingart, *J. Electrochem. Soc.*, 2010, **157**, A1279–A1286.

2 Y. Ito, M. Nyce, R. Plivelich, M. Klein and D. Steingart, *J. Power Sources*, 2011, **196**, 2340–2345.

3 A. Radisic, P. M. Vereecken, J. B. Hannon, P. C. Searson and F. M. Ross, *Nano Lett.*, 2006, **6**, 238–242.

4 K. Karki, G. G. Amatucci, M. S. Whittingham and F. Wang, *Microsc. Microanal.*, 2014, **20**, 512–513.

5 D. Santhanagopalan, D. Qian, T. McGilvray, Z. Wang, F. Wang, F. Camino, J. Graetz, N. Dudney and Y. S. Meng, *J. Phys. Chem. Lett.*, 2014, **5**, 298–303.

6 F. Marone and M. Stampanoni, *Adv. Energy Mater.*, 2013, **3**, 845–850.

7 X. Liu, D. Wang, G. Liu, V. Srinivasan, Z. Liu, Z. Hussain and W. Yang, *Nat. Commun.*, 2013, **4**, 2568.

8 Y.-C. K. Chen-Wiegart, J. Wang and J. Wang, *SPIE Optical Engineering + Applications*, International Society for Optics and Photonics, 2013, p. 88510C.

9 J. Nelson, S. Misra, Y. Yang, A. Jackson, Y. Liu, H. Wang, H. Dai, J. C. Andrews, Y. Cui and M. F. Toney, *J. Am. Chem. Soc.*, 2012, **134**, 6337–6343.

10 G. Du, N. Sharma and V. K. Peterson, *Adv. Funct. Mater.*, 2011, **21**, 3990–3997.

11 I. Manke, J. Banhart, A. Haibel, A. Rack, S. Zabler, N. Kardjilov, A. Hilger, A. Melzer and H. Riesemeier, *Appl. Phys. Lett.*, 2007, **90**, 214102.

12 A. R. Armstrong, M. Holzapfel and P. Novák, *J. Am. Chem. Soc.*, 2006, **128**, 8694–8698.

13 J. W. Gallaway, C. K. Erdonmez, Z. Zhong, M. Croft, L. A. Sviridov, T. Z. Sholklapper, D. E. Turney, S. Banerjee and D. A. Steingart, *J. Mater. Chem. A*, 2014, **2**, 2757–2764.

14 J. W. Gallaway, M. Menard, B. Hertzberg, Z. Zhong, M. Croft, L. A. Sviridov, D. E. Turney, S. Banerjee, D. A. Steingart and C. K. Erdonmez, *J. Electrochem. Soc.*, 2015, **162**, A162–A168.

15 J. Rijssenbeek, Y. Gao, Z. Zhong, M. Croft, N. Jisrawi, A. Ignatov and T. Tsakalakos, *J. Power Sources*, 2011, **196**, 2332–2339.

16 A. Senyshyn, M. J. Mühlbauer, K. Nikolowski, T. Pirling and H. Ehrenberg, *J. Power Sources*, 2012, **203**, 126–129.

17 J. Cannarella and C. B. Arnold, *J. Power Sources*, 2014, **245**, 745–751.

18 J. Cannarella and C. B. Arnold, *J. Power Sources*, 2013, **226**, 149–155.

19 J. Cannarella and C. B. Arnold, *J. Power Sources*, 2014, **269**, 7–14.

20 G. Y. Gor, J. Cannarella, J. H. Prévost and C. B. Arnold, *J. Electrochem. Soc.*, 2014, **161**, F3065–F3071.

21 R. Deshpande, M. Verbrugge, Y.-T. Cheng, J. Wang and P. Liu, *J. Electrochem. Soc.*, 2012, **159**, A1730–A1738.

22 Y. Koyama, T. E. Chin, U. Rhyner, R. K. Holman and S. R. Hall, *Adv. Funct. Mater.*, 2006, **16**, 492–498.

23 S. Didier-Laurent, H. Idrissi and L. Roué, *J. Power Sources*, 2008, **179**, 412–416.

24 A. Etiemble, H. Idrissi, S. Meille and L. Roué, *J. Power Sources*, 2012, **205**, 500–505.

25 S. Komagata, N. Kuwata, R. Baskaran, J. Kawamura, K. Sato and J. Mizusaki, *ECS Trans.*, 2010, **25**, 163–167.

26 N. Kircheva, S. Genies, D. Brun-Buisson and P.-X. Thivel, *J. Electrochem. Soc.*, 2011, **159**, A18–A25.

27 K. Rhodes, M. Kirkham, R. Meisner, C. M. Parish, N. Dudney and C. Daniel, *Rev. Sci. Instrum.*, 2011, **82**, 075107.

28 K. Rhodes, N. Dudney, E. Lara-Curzio and C. Daniel, *J. Electrochem. Soc.*, 2010, **157**, A1354–A1360.

29 W. H. Woodford, Y.-M. Chiang and W. C. Carter, *J. Mech. Phys. Solids*, 2014, **70**, 71–83.

30 W. H. Woodford, W. Craig Carter and Y.-M. Chiang, *Energy Environ. Sci.*, 2012, **5**, 8014–8024.

31 W. H. Woodford, Y.-M. Chiang and W. C. Carter, *J. Electrochem. Soc.*, 2010, **157**, A1052–A1059.

32 W. H. Woodford, W. C. Carter and Y.-M. Chiang, *J. Electrochem. Soc.*, 2014, **161**, F3005–F3009.

33 B. Sood, M. Osterman and M. Pecht, *Product Compliance Engineering (ISPCE), 2013 IEEE Symposium on*, 2013, pp. 1–6.

34 B. Sood, C. Hendricks, M. Osterman and M. Pecht, *International Symposium for Testing and Failure Analysis (ISTFA)*, 2013, pp. 4–16.

35 *Non-Contact Ultrasonic Evaluation of Prismatic Lithium Ion Battery Cells*, The Ultran Group, 2012, http://www.ultrangroup.com/index.php/jec-europe-2013/.

36 E. S. Furgason, V. L. Newhouse, N. M. Bilgutay and G. R. Cooper, *Ultrasonics*, 1975, **13**, 11–17.

37 B. Banks, *Ultrasonics*, 1963, **1**, I.

38 A. Vary, *Acousto-ultrasonic characterization of fiber reinforced composites*, NASA, 1982.

39 R. LeVeque, Clawpack Development Team, Clawpack Version 5.2.2, 2014, http://www.clawpack.org/.

40 J. N. Reimers and J. R. Dahn, *J. Electrochem. Soc.*, 1992, **139**, 2091–2097.

41 T. Reddy and J. Linden, *Handbook of Batteries*, McGraw-Hill, 2004, vol. III.

42 F. T. Schulitz, Y. Lu and H. N. G. Wadley, *J. Acoust. Soc. Am.*, 1998, **103**, 1361–1369.

43 D. J. McClements, *Adv. Colloid Interface Sci.*, 1991, **37**, 33–72.

44 R. E. Challis, M. J. W. Povey, M. L. Mather and A. K. Holmes, *Rep. Prog. Phys.*, 2005, **68**, 1541.

45 P. Albertus and J. Newman, Introduction to Dualfoil 5.0, University of California, Berkeley, Tech. Rep., 2007.

46 D. Steingart, GitHub.

47 J. D. N. Cheeke, *Fundamentals and applications of ultrasonic waves*, CRC Press, 2012.

48 A. Van der Ven, M. K. Aydinol, G. Ceder, G. Kresse and J. Hafner, *Phys. Rev. B: Condens. Matter Mater. Phys.*, 1998, **58**, 2975–2987.

49 T. P. Dirkse, C. Postmus and R. Vandenbosch, *J. Am. Chem. Soc.*, 1954, **76**, 6022–6024.

50 S. Szpak and C. J. Gabriel, *J. Electrochem. Soc.*, 1979, **126**, 1914–1923.

51 S. Bhadra, B. J. Hertzberg, A. G. Hsieh, M. Croft, J. W. Gallaway, B. J. Van Tassell, M. Chamoun, C. Erdonmez, Z. Zhong, T. Sholklapper and D. A. Steingart, *J. Mater. Chem. A*, 2015, DOI: 10.1039/C5TA01576F.

52 G. V. Riley, D. S. Hussey and D. Jacobson, *ECS Trans.*, 2010, **25**, 75–83.

53 Q. C. Horn and Y. Shao-Horn, *J. Electrochem. Soc.*, 2003, **150**, A652–A658.

54 B. Carter, *Battery Manufacturing in the US Market Research*, IBISworld, 2014.

55 L. M. Pearce, *Encyclopedia of American Industries*, 6th edn, Gale, 2009.

56 M. Anderman, *The Tesla Battery Report 2014 – Overview – Advanced Automotive Batteries*, Advanced Automotive Batteries, 2014.